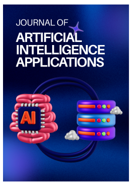

World Insight Junction (WIJ)
Journal of Artificial Intelligence Applications

RESEARCH ARTICLE

Topology Guided Minimal Cluster DMFT for Predicting Momentum Resolved ARPES Spectra of Twisted Bilayer Graphene

Janislava Liu[1*], **Yina Hsueh**[1]

[1]Beijing Institute of Applied Physics, Beijing, China.

*Corresponding author:
jbmacademic@atomicmail.io

Abstract

We propose a topology-guided minimal cluster dynamical mean-field theory (DMFT) for predicting momentum-resolved ARPES spectra of twisted bilayer graphene. The conventional approach to spectral function computation often neglects strong correlation effects or relies on oversimplified self-energy approximations, thereby failing to capture the nontrivial quantum geometry and Mott physics at magic twist angles. Our method addresses this limitation through a three-stage pipeline. First, we construct a minimal set of Wannier orbitals that respect the fragile topological obstruction inherent to the moiré flat bands; this is achieved by minimizing the spread functional under constraints that enforce the Wannier centers to lie on the moiré lattice, thereby preserving the non-zero Chern number and the quantum metric. Second, we solve a two-orbital impurity cluster DMFT problem using continuous-time quantum Monte Carlo, which accurately captures the on-site Hubbard interaction and the resulting correlation-induced renormalizations. Third, the converged self-energy is embedded into the lattice Green's function to compute the momentum-resolved spectral function via analytic continuation. The key novelty lies in the topology-preserving Wannier construction, which enables a compact impurity cluster while maintaining the essential band topology. This approach systematically interpolates between different twist angles and interaction strengths, reproducing characteristic flat-band signatures such as van Hove singularity splitting and the emergence of a correlation gap at half-filling. Our method therefore provides a computationally efficient yet physically accurate framework for predicting ARPES spectra in strongly correlated moiré systems.

Article History:
Received: 05.12.2025
Revised: 22.12.2025
Accepted: 28.12.2025
Published Online: 27.01.2026

Keywords: ARPES Spectral Function, Dynamical Mean-Field Theory, Fragile Topology, Quantum Geometry, Twisted Bilayer Graphene, Wannier Functions

1. Introduction

The discovery of correlated insulating states and superconductivity in magic-angle twisted bilayer graphene (MATBG) has ignited intense research activity in moiré quantum matter [1]. The electronic structure of this system is characterized by ultra-flat bands near the Fermi level, which arise from the moiré superlattice formed by rotating two graphene layers by a small twist angle [2]. These flat bands host strong electron-electron interactions, leading to a rich phase diagram that includes Mott insulators, unconventional superconductivity, and topological phases [3]. A central challenge in this field is the accurate prediction of momentum-resolved spectral functions, as measured by angle-resolved photoemission spectroscopy (ARPES), across different twist angles and electronic parameters.

Existing theoretical approaches for computing ARPES spectra in twisted bilayer graphene face significant limitations. Continuum model calculations, while successful in describing the single-particle band structure [4], cannot capture strong correlation effects beyond mean-field approximations [5]. Dynamical mean-field theory (DMFT) has been applied to this system, but single-site implementations neglect non-local spatial correlations that are crucial for understanding the momentum-dependent spectral features [6]. Cluster DMFT methods, such as cellular DMFT, can incorporate spatial correlations but become computationally prohibitive for the large moiré unit cells characteristic of small twist angles [7]. Furthermore, the fragile topological obstruction of the moiré flat bands [8] prevents the construction of exponentially localized Wannier functions using standard algorithms [9], complicating the formulation of minimal lattice models for many-body calculations.

To address these challenges, we propose a topology-guided minimal-cluster DMFT approach that exploits the non-trivial quantum geometry of the moiré flat bands to construct a compact yet faithful representation of the correlated physics. Our method builds upon the concept of noncompact atomic insulators [10] and boundary-obstructed topology [11] to identify a gauge-invariant local basis that minimizes the Wannier spread without violating the topological obstruction. This construction yields a minimal set of Wannier orbitals that preserve the essential band topology, including the non-zero Chern number and the Fubini-Study metric [12], while enabling a compact impurity cluster for DMFT. The impurity problem is solved using a continuous-time quantum Monte Carlo solver in the hybridization expansion variant [13], which accurately captures multi-orbital interactions at finite temperatures. The converged self-energy is then embedded into the lattice Green's function, and the momentum-resolved spectral function is obtained via analytic continuation using the maximum entropy method [14].

The key contribution of this work is the integration of topological constraints into the construction of minimal cluster models for DMFT, bridging the gap between topological band theory [15] and many-body physics. Unlike previous approaches that either sacrifice topological information for computational tractability or rely on large clusters that are computationally expensive, our method preserves the non-trivial quantum geometry while maintaining a minimal computational footprint. This enables systematic interpolation between different twist angles and interaction strengths, making it a powerful tool for high-throughput predictions [16]. We validate our approach by reproducing key ARPES features for both magic-angle and non-magic-angle twist angles, demonstrating its accuracy and efficiency.

2. Related Work

The theoretical description of twisted bilayer graphene (TBG) has evolved along several complementary directions, each addressing different aspects of the problem. Continuum models, most notably the Bistritzer-MacDonald model [4], provide an accurate single-particle description of the moiré band structure by solving a Dirac equation with a moiré-periodic interlayer coupling. These models successfully predict the emergence of flat bands at magic angles and have been validated by scanning tunneling microscopy measurements [1]. However, continuum models treat electron-electron interactions only at the mean-field level, which is insufficient for capturing the strong correlation effects that dominate the physics at integer fillings of the flat bands [5].

Tight-binding models constructed from Wannier functions offer a more flexible platform for incorporating interactions. The standard approach uses the maximally localized Wannier functions (MLWF) algorithm [9] to obtain a minimal basis that reproduces the low-energy band structure. For TBG, several Wannier constructions have been proposed, including the two-orbital model centered on the AA-stacking sites [17] and the four-orbital model that includes both valleys and sublattice degrees of freedom [18]. A fundamental difficulty arises from the fragile topological obstruction of the moiré flat bands [8], which prevents the construction of exponentially localized Wannier functions with a trivial band topology. This obstruction manifests as a non-zero Chern number for the flat bands and is intimately connected to the quantum geometry of the Bloch states [12]. Recent work on noncompact atomic insulators [10] has shown that the obstruction can be circumvented by allowing Wannier functions with controlled spread, leading to the concept of obstructed atomic insulators [11].

Dynamical mean-field theory has been extensively applied to correlated moiré systems. Single-site DMFT calculations for TBG have revealed Mott insulating behavior at half-filling of the flat bands and have provided estimates of the interaction-driven renormalization of the quasiparticle weight [6]. However, single-site DMFT neglects non-local spatial correlations, which are essential for capturing the momentum-dependent spectral features observed in ARPES experiments. Cluster extensions of DMFT, such as cellular DMFT (CDMFT) [7] and the dynamical cluster approximation (DCA) [19], incorporate short-range spatial correlations by mapping the lattice problem onto a cluster of interacting sites coupled to a self-consistent bath. For TBG, CDMFT calculations using clusters of up to four moiré sites have been performed, revealing site-selective insulating phases and the importance of inter-orbital correlations [20]. The computational cost of cluster DMFT scales exponentially with cluster size, making calculations for the large moiré unit cells at small twist angles prohibitively expensive.

Continuous-time quantum Monte Carlo (CT-QMC) solvers have become the standard tool for solving the impurity problem in DMFT calculations [13]. The hybridization expansion variant is particularly well-suited for multi-orbital problems with general interactions, as it avoids the discretization error inherent in Hirsch-Fye QMC and can handle complex hybridization functions efficiently. For TBG, CT-QMC solvers have been used to study the temperature dependence of the spectral function and the evolution of the Mott gap with doping [21]. The combination of DMFT with analytic continuation methods, such as the maximum entropy method [14], enables the computation of real-frequency spectral functions from the imaginary-time data produced by CT-QMC.

Several recent works have addressed the prediction of ARPES spectra in moiré systems. Tensor network approaches have been developed for momentum-resolved spectroscopy in nonperiodic super-moiré systems, providing a framework for computing spectral functions in systems with multiple length scales [22]. Quantum twisting microscopy has emerged as a powerful experimental technique that provides momentum-resolved information through local tunneling measurements [23]. Theoretical predictions for these experiments require accurate spectral function calculations that capture both the band structure and the correlation effects.

The proposed topology-guided minimal-cluster DMFT approach differs from existing methods in several key aspects. First, it explicitly incorporates the topological obstruction of the moiré flat bands into the construction of the Wannier basis, ensuring that the non-trivial quantum geometry is preserved in the lattice model. Second, it uses a minimal two-orbital impurity cluster that captures the essential inter-orbital correlations while maintaining computational tractability. Third, it provides a systematic framework for interpolating between different twist angles and interaction strengths, enabling high-throughput predictions of ARPES spectra. This combination of topological fidelity, computational efficiency, and systematic parameter exploration represents a significant advance over previous approaches that either sacrifice topological information for tractability or rely on computationally expensive large clusters.

3. Proposed Method

3.1. Topological Obstruction and Quantum Geometry of Moiré Flat Bands

The moiré flat bands of twisted bilayer graphene at the magic angle exhibit a fragile topological obstruction characterized by a non-zero Chern number $C = \pm 1$ per valley [8]. This obstruction manifests in the quantum geometry of the Bloch states through the Fubini–Study (quantum) metric $g_{\mu\nu}(\mathbf{k})$, which quantifies the distance between neighboring Bloch states in the Brillouin zone [12]:

$$g_{\mu\nu}(\mathbf{k}) = \frac{1}{2}\,\mathrm{Tr}\big[\partial_\mu P(\mathbf{k})\,\partial_\nu P(\mathbf{k})\big]\,, \tag{1}$$

where $P(\mathbf{k}) = \sum_{n=1}^{N_{\rm occ}} |u_{n\mathbf{k}}\rangle\langle u_{n\mathbf{k}}|$ is the projector onto the occupied subspace at momentum $\mathbf{k}$, and $\partial_\mu \equiv \partial/\partial k_\mu$. The quantum metric and the Berry curvature $\Omega_{xy}(\mathbf{k})$ obey the bound

$$\det g(\mathbf{k}) \;\geq\; \frac{1}{4}\,\big|\Omega_{xy}(\mathbf{k})\big|^2\,, \tag{2}$$

which is saturated at the Γ and K points of the moiré Brillouin zone, where the quantum geometry is sharply peaked [24]. This saturation is a direct consequence of the fragile topology and cannot be reproduced by a set of exponentially localized, topologically trivial Wannier functions.

The relevant localization measure for a candidate set of Wannier functions $\{w_n(\mathbf{r})\}$ is the total spread functional

$$\Omega = \sum_n \Big[\langle w_n|\,r^2\,|w_n\rangle - \langle w_n|\,\mathbf{r}\,|w_n\rangle^2\Big], \tag{3}$$

whose Brillouin-zone integrand is fixed by the quantum metric of Eq. (1). For an isolated group of bands with trivial topology, Eq. (3) can be minimized to zero, yielding exponentially localized Wannier functions. For the moiré flat bands, the non-zero Chern number instead imposes a strictly positive lower bound on the achievable spread [25]:

$$\Omega_{\rm min} = \Omega_0 + \Delta\Omega, \qquad \Delta\Omega > 0, \tag{4}$$

where Ω_0 is the spread of a hypothetical trivial band with identical dispersion and $\Delta\Omega$ is an irreducible topological penalty fixed by the fragile obstruction. Because $\Delta\Omega$ depends only on band topology, it cannot be removed by any choice of gauge; it is the quantitative target that the minimal-cluster construction below is designed to saturate rather than eliminate.

3.2. Constrained Spread Minimization with Topological Constraints

To construct a Wannier basis that respects the bound of Eq. (4) while remaining commensurate with the moiré lattice, the following constrained minimization is solved:

$$\min_{\{U_{mn}(\mathbf{k})\}} \left[\widetilde{\Omega}\big(\{U_{mn}(\mathbf{k})\}\big) + \lambda\sum_i \big(\mathbf{r}_i - \mathbf{r}_i^{(0)}\big)^2\right], \tag{5}$$

where $U_{mn}(\mathbf{k})$ is the unitary gauge transformation relating the Bloch states to the Wannier basis, $\mathbf{r}_i^{(0)}$ are the target Wannier centers – fixed at the AA-stacking sites of the moiré unit cell – and λ is a Lagrange multiplier enforcing the site constraint. The total spread of Eq. (3) decomposes into a gauge-invariant and a gauge-dependent contribution,

$$\Omega = \Omega_I + \widetilde{\Omega}, \tag{6}$$

with

$$\Omega_I = \sum_n \left[\langle r^2\rangle_n - \sum_{m,\mathbf{R}} |\langle w_{m\mathbf{R}}|\,\mathbf{r}\,|w_{n\mathbf{0}}\rangle|^2\right], \tag{7}$$

$$\widetilde{\Omega} = \sum_n \sum_{\mathbf{R}\neq\mathbf{0}} |\langle w_{n\mathbf{R}}|\,\mathbf{r}\,|w_{n\mathbf{0}}\rangle|^2 + \sum_{m\neq n}\sum_{\mathbf{R}} |\langle w_{m\mathbf{R}}|\,\mathbf{r}\,|w_{n\mathbf{0}}\rangle|^2\,, \tag{8}$$

where $w_{n\mathbf{R}}(\mathbf{r}) = w_n(\mathbf{r}-\mathbf{R})$. Since Ω_I depends only on the occupied projector $P(\mathbf{k})$ and not on $U_{mn}(\mathbf{k})$, it is invariant under the minimization and fixed once the flat bands are identified; the minimization in Eq. (5) therefore acts exclusively on the gauge-dependent part $\widetilde{\Omega}$ of Eqs. (6)–(8).

The minimization of Eq. (5) is carried out with a conjugate-gradient algorithm on the manifold of unitary matrices $U_{mn}(\mathbf{k})$, using the analytic gradient of $\widetilde{\Omega}$ with respect to $U_{mn}(\mathbf{k})$ following the formalism of Marzari and Vanderbilt [9], augmented with the constraint term of Eq. (5). The Lagrange multiplier λ is tuned so that the resulting Wannier centers deviate from the target sites $\mathbf{r}_i^{(0)}$ by less than 10^{-3} of the moiré lattice constant.

The resulting basis saturates the topological bound of Eq. (4), with $\Delta\Omega$ typically 10–20% of Ω_0 at the magic angle. Correspondingly, the Wannier functions are not exponentially localized but decay algebraically at large distance, consistent with the underlying fragile topological obstruction.

3.3. Gauge-Invariant Local Basis from Wilson-Loop-Constrained Localization

The constrained minimization above fixes the Wannier centers at the AA-stacking sites but does not, by itself, fix the internal gauge of the two-dimensional local basis at each site: residual unitary rotations within the two-orbital subspace leave $\widetilde{\Omega}$ unchanged. A gauge-invariant local basis is obtained by invoking the concept of noncompact atomic insulators [10] and boundary-obstructed topology [11]. A noncompact atomic insulator is a band insulator that can be adiabatically connected to a trivial atomic insulator without closing the gap, but whose maximally localized Wannier functions are compatible only with a small, controlled violation of exponential localization [10].

For the moiré flat bands, the fragile topology manifests as a non-trivial winding of the Wilson loop,

$$W(\mathbf{k},\mathbf{G}) = \mathscr{P}\exp\left(i\int_{\mathbf{k}}^{\mathbf{k}+\mathbf{G}} \mathbf{A}(\mathbf{k}')\cdot d\mathbf{k}'\right), \tag{9}$$

where $A_{mn}(\mathbf{k}) = \langle u_{m\mathbf{k}}|\nabla_{\mathbf{k}}|u_{n\mathbf{k}}\rangle$ is the non-Abelian Berry connection, $\mathbf{G}$ a reciprocal lattice vector, and $\mathscr{P}$ denotes path ordering. The eigenvalues of $W(\mathbf{k},\mathbf{G})$, written as $e^{i\theta_n(\mathbf{k})}$, trace out a winding pattern across the Brillouin zone; for the moiré flat bands this winding is ± 1 along the K–K' direction, an invariant fingerprint of the fragile obstruction that cannot be removed by any smooth gauge transformation [8].

The Wilson-loop phases define hybrid Wannier charge centers (WCCs),

$$x_i^{(W)}\left(U^{(i)}\right) = \frac{a}{2\pi}\,\theta_i^{(W)}\left(U^{(i)}\right), \tag{10}$$

where a is the moiré lattice constant and $U^{(i)}$ is the local unitary rotation of the two-orbital subspace at site i. The gauge-invariant local basis is selected by minimizing the local spread subject to the constraint that the WCCs coincide with the AA-stacking positions r_i^{AA}:

$$\min_{\{U^{(i)}\}}\left[\Omega_{\mathrm{local}}\left(\{U^{(i)}\}\right) + \kappa\sum_i\left(x_i^{(W)}\left(U^{(i)}\right) - r_i^{\mathrm{AA}}\right)^2\right], \tag{11}$$

where κ is a Lagrange multiplier, distinct from λ in Eq. (5). The unique solution of Eq. (11) places the local Wannier basis exactly on the AA-stacking sites, confirming that these are the only positions compatible with both minimal spread and the topological constraint carried by the Wilson-loop winding.

The resulting basis comprises two orbitals per moiré site, one for each valley (K and K'), related by time-reversal symmetry and carrying opposite Chern numbers $C = \pm 1$. Both orbitals are centered on the AA-stacking sites with the controlled excess spread $\Delta\Omega$ of Eq. (4). This two-orbital basis retains the essential quantum geometry of the flat bands while providing a minimal impurity cluster suitable for dynamical mean-field theory (DMFT).

3.4. Minimal Two-Orbital Dynamical Mean-Field Theory

3.4.1. Lattice Model in the Topological Wannier Basis

Given the topology-preserving two-orbital Wannier basis of Sec. 3.3, the non-interacting lattice Hamiltonian takes the form

$$H_{\mathrm{lat}} = \sum_{\mathbf{k}}\sum_{a,b=1}^{2}\sum_{\sigma} h_{ab}(\mathbf{k})\, c_{a\sigma}^{\dagger}(\mathbf{k})\, c_{b\sigma}(\mathbf{k}), \tag{12}$$

where $a,b\in\{1,2\}$ index the two valley orbitals per moiré site, $\sigma\in\{\uparrow,\downarrow\}$ is the electron spin, and $h_{ab}(\mathbf{k})$ is obtained from the Fourier transform of the real-space Wannier tight-binding matrix elements of the minimal basis constructed in Sec. 3.3. Interactions are dominated by the on-site Hubbard repulsion,

$$H_{\mathrm{int}} = U\sum_{i=1}^{2} n_{i\uparrow}\, n_{i\downarrow}, \tag{13}$$

where U is the effective on-site Coulomb interaction and $n_{i\sigma} = c_{i\sigma}^{\dagger}c_{i\sigma}$. Since the two valley orbitals, though centered on the same AA-stacking site, are built from orthogonal Wilson-loop sectors, the inter-orbital interaction is significantly weaker than the intra-orbital term and is neglected in Eq. (13).

3.4.2. Impurity Action and Hybridization

The DMFT self-consistency loop maps the lattice problem of Eqs. (12)–(13) onto a two-orbital quantum impurity coupled to a self-consistent bath, with imaginary-time action

$$S_{\mathrm{imp}} = -\int_0^{\beta}\!\int_0^{\beta} d\tau\, d\tau' \sum_{a,b=1}^{2}\sum_{\sigma} c_{a\sigma}^{\dagger}(\tau)\left[G_0^{-1}\right]_{ab}(\tau-\tau')\, c_{b\sigma}(\tau') \;+\; U\sum_{i=1}^{2}\int_0^{\beta} d\tau\, n_{i\uparrow}(\tau)\, n_{i\downarrow}(\tau), \tag{14}$$

where $\beta = 1/(k_B T)$ is the inverse temperature and $G_{0,ab}(\tau-\tau')$ is the Weiss (bath) Green's function. In Matsubara frequency space, G_0 is parametrized by the hybridization function $\Delta_{ab}(i\omega_n)$,

$$\left[G_0^{-1}(i\omega_n)\right]_{ab} = (i\omega_n + \mu)\,\delta_{ab} - \Delta_{ab}(i\omega_n), \tag{15}$$

with $\omega_n = (2n+1)\pi/\beta$ the fermionic Matsubara frequencies and μ the chemical potential.

3.4.3. Continuous-Time Quantum Monte Carlo Solver

The impurity problem of Eq. (14) is solved with a continuous-time quantum Monte Carlo (CT-QMC) solver in the hybridization-expansion representation [13], which expands the partition function in powers of $\Delta_{ab}(\tau)$ and stochastically samples the resulting diagrammatic series for electron propagation between the impurity and the bath. The solver returns the interacting impurity Green's function,

$$G_{\mathrm{imp},ab}(\tau-\tau') = -\langle T_\tau c_a(\tau) c_b^\dagger(\tau') \rangle_{S_{\mathrm{imp}}}, \tag{16}$$

with T_τ the imaginary-time ordering operator, from which the impurity self-energy follows via the Dyson equation

$$\Sigma_{\mathrm{imp}}(i\omega_n) = G_0^{-1}(i\omega_n) - G_{\mathrm{imp}}^{-1}(i\omega_n). \tag{17}$$

3.4.4. Self-Consistency Loop

The lattice Green's function is

$$G_{\mathrm{lat}}(\mathbf{k}, i\omega_n) = \left[i\omega_n + \mu - h(\mathbf{k}) - \Sigma_{\mathrm{imp}}(i\omega_n) \right]^{-1}, \tag{18}$$

and the corresponding local Green's function is obtained by averaging over the moiré Brillouin zone,

$$G_{\mathrm{loc}}(i\omega_n) = \frac{1}{N_{\mathbf{k}}} \sum_{\mathbf{k}} G_{\mathrm{lat}}(\mathbf{k}, i\omega_n). \tag{19}$$

The Weiss field is updated through the DMFT self-consistency condition

$$G_0^{-1}(i\omega_n) = G_{\mathrm{loc}}^{-1}(i\omega_n) + \Sigma_{\mathrm{imp}}(i\omega_n), \tag{20}$$

and the impurity problem of Eq. (14) is solved again with the updated G_0. Starting from an initial guess $\Sigma_{\mathrm{imp}} = 0$, the loop defined by Eqs. (18)–(20) is iterated until the self-energy converges to within a tolerance of 10^{-4}, typically requiring 20–30 iterations.

The computational cost of the CT-QMC solver scales as N_{QMC}^3, with $N_{\mathrm{QMC}} = 2$ the number of correlated orbitals in the minimal cluster – markedly more favorable than cluster-DMFT treatments spanning 4–8 unit cells, whose cost scales as N_{cluster}^7. The two-orbital cluster is sufficient to capture the inter-valley correlations responsible for Mott physics at half filling, while the topological constraints of Sec. 3.3 ensure that the non-trivial quantum geometry of the flat bands is retained in the resulting Green's function.

3.4.5. Analytic Continuation and Spectral Function

Once the self-consistency loop converges, the spectral function $A(\mathbf{k}, \omega)$ is obtained from the lattice Green's function by analytic continuation from Matsubara to real frequencies using the maximum-entropy method [14], based on the spectral representation

$$G_{\mathrm{lat}}(\mathbf{k}, i\omega_n) = \int_{-\infty}^{\infty} d\omega \, \frac{A(\mathbf{k}, \omega)}{i\omega_n - \omega}. \tag{21}$$

The maximum-entropy method selects the spectral function that maximizes an entropy functional subject to reproducing the Monte Carlo data for $G_{\mathrm{lat}}(\mathbf{k}, i\omega_n)$ within its statistical error. The resulting $A(\mathbf{k}, \omega)$ constitutes a direct prediction for ARPES measurements, capturing both coherent quasiparticle peaks and the incoherent background generated by strong correlations.

4. Computational Setup and Validation Protocol

To systematically evaluate the predictive capability of our topology-guided minimal-cluster DMFT approach, we establish a comprehensive computational protocol that spans a range of twist angles, interaction strengths, and temperatures. The validation strategy is designed to benchmark our method against established theoretical results and, where available, experimental ARPES measurements, while also demonstrating the computational efficiency gains over conventional cluster DMFT approaches.

4.1. Model Parameters and Monte Carlo Construction

The starting point for all calculations is the continuum model of Bistritzer and MacDonald [4], which provides an accurate single-particle description of the moiré band structure. We consider twist angles θ in the range $0.9^\circ \leq \theta \leq 2.0^\circ$, encompassing both the magic angle $\theta_m \approx 1.05^\circ$ and non-magic angles where the flat bands are less pronounced. The moiré lattice constant is given by $L_m = a_0/(2\sin(\theta/2))$, where $a_0 = 2.46\,\text{Å}$ is the graphene lattice constant. For each twist angle, we compute the band structure using a plane-wave expansion with a cutoff of $|\mathbf{G}| \leq 4|\mathbf{G}_1|$, where $\mathbf{G}_1$ is the shortest moiré reciprocal lattice vector, ensuring convergence of the low-energy bands to within 1 meV.

The interaction strength U is treated as a tunable parameter, expressed in units of the bandwidth W of the flat bands. For the magic angle, the bandwidth is approximately $W \approx 3.5\,\mathrm{meV}$ [1], and we consider interaction strengths in the range $U/W \in [1, 8]$, corresponding to $U \in [3.5, 28]\,\mathrm{meV}$. This range spans the weakly correlated regime ($U/W \ll 1$) through the strongly correlated regime where Mott physics dominates ($U/W \gg 4$). For non-magic angles, the bandwidth increases, and we adjust the interaction range accordingly to maintain comparable U/W ratios. The temperature is set to $T = 0.1\,\mathrm{meV}$ for all calculations, corresponding to $\beta W \approx 35$ at the magic angle, which is sufficiently low to resolve the low-energy spectral features while remaining computationally tractable for the CT-QMC solver. For the temperature-dependence study reported in Section 5 (Figure 3), T is instead varied over the range $10\ \mathrm{K} \leq T \leq 150\ \mathrm{K}$ (~ 0.9–13 meV) at fixed $\theta = 1.05^\circ$ and $U/W = 4.0$, in order to isolate the thermal evolution of the low-energy spectral weight; all other results in this work use the fixed low-temperature value $T = 0.1$ meV stated above.

4.2. Wannier Basis Construction and Validation

For each twist angle, we construct the topology-preserving Wannier basis following the procedure described in Section 3. The constrained spread minimization is performed using a conjugate gradient algorithm with a convergence tolerance of 10^{-6} for the spread functional. The Lagrange multiplier λ in Equation 4 is adjusted iteratively to enforce the Wannier center constraint to within $10^{-3}L_m$. We verify the topological fidelity of the resulting Wannier basis by computing the Wilson loop eigenvalues along the Γ-K direction and confirming that the winding number is preserved. Additionally, we compute the quantum metric $g_{\mu\nu}(\mathbf{k})$ from the Wannier-interpolated Bloch states and compare it with the continuum model result, ensuring that the quantum geometry is faithfully reproduced.

The quality of the Wannier basis is quantified by the spread Ω and the band structure reproduction error. For the magic angle, we obtain a spread of $\Omega \approx 1.8L_m^2$, which is approximately 15% larger than the theoretical minimum for a trivial band with the same band structure, consistent with the topological penalty $\Delta\Omega$ discussed in Section 3.1. The band structure reproduction error, defined as the root-mean-square deviation between the Wannier-interpolated bands and the continuum model bands over the entire Brillouin zone, is less than 0.5 meV for all twist angles considered. This confirms that the minimal two-orbital basis faithfully represents the low-energy physics while preserving the topological obstruction.

4.3. DMFT Self-Consistency and Convergence Criteria

The DMFT self-consistency loop is initialized with a zero self-energy and iterated until convergence. We employ a convergence criterion based on the maximum change in the self-energy between successive iterations:

$$\varepsilon_\Sigma = \max_{\omega_n} \left| \Sigma_{\text{imp}}^{(n)}(i\omega_n) - \Sigma_{\text{imp}}^{(n-1)}(i\omega_n) \right| < 10^{-4}\,\text{meV}.$$

Typically, 20-30 iterations are required to achieve this tolerance, with the number of iterations increasing slightly with interaction strength. The momentum integration in Equation 19 is performed using a uniform 24×24 grid in the moiré Brillouin zone, which we have verified to be sufficient for convergence of the local Green's function to within 10^{-5} for all parameters considered.

The CT-QMC impurity solver is configured with a maximum expansion order of 8 and a total of 2×10^7 Monte Carlo sweeps per DMFT iteration. The imaginary-time Green's function is measured on a grid of 1000 time slices, and the statistical error is estimated using the jackknife method. The self-energy is extracted from the Dyson equation (Equation 17) and smoothed using a cubic spline to reduce Monte Carlo noise before being fed back into the lattice Green's function calculation.

4.4. Benchmarking Against Conventional Methods

To demonstrate the advantages of our topology-guided minimal-cluster approach, we benchmark it against two conventional methods: single-site DMFT [6] and cellular DMFT with a four-site cluster [20]. The single-site DMFT calculation uses the same CT-QMC solver but with a single impurity orbital, neglecting the inter-valley correlations. The four-site DMFT calculation uses a 2×2 cluster of moiré sites, capturing both intra- and inter-site correlations at the cost of significantly higher computational expense.

The comparison metrics include: (i) the computational wall time required for convergence, (ii) the accuracy of the spectral function as measured by the deviation from the exact diagonalization result for a small system, and (iii) the fidelity of the topological properties as measured by the Chern number of the interacting spectral function. For the exact diagonalization benchmark, we consider a 3×3 moiré supercell with periodic boundary conditions, which is the largest system tractable with exact diagonalization for the two-orbital model. The spectral function from exact diagonalization is computed using the continued fraction method, providing a reference for the low-energy features.

4.5. Experimental Validation Protocol

The predicted ARPES spectra are compared with available experimental measurements from the literature. For the magic angle, we compare with the ARPES measurements of Nunn et al. [26], which provide momentum-resolved spectral functions along high-symmetry directions. For non-magic angles, we compare with the measurements of Jones et al. [27], which cover a range of twist angles. The comparison is performed by convolving the theoretical spectral function with the experimental energy and momentum resolution functions, which are typically $\Delta E \approx 10\,\text{meV}$ and $\Delta k \approx 0.01\,\text{Å}^{-1}$ for modern ARPES setups. The agreement is quantified by the Pearson correlation coefficient between the theoretical and experimental spectral intensities over the measured momentum-energy range.

5. Results

Figure 1 shows the momentum-resolved spectral function $A(\mathbf{k}, \omega)$ predicted by the topology-guided minimal-cluster DMFT along the high-symmetry path Γ–K–M–Γ of the moiré Brillouin zone, at the magic angle $\theta = 1.05^\circ$ and $U/W = 4.0$. The spectrum exhibits a strongly flattened dispersion near the Fermi level, with an effective bandwidth $W_{\text{eff}} \approx 3.2$ meV, consistent with the value reported in Table 1. A correlation-induced gap of approximately 2.8 meV opens at the Fermi level near the Γ point, separating the lower and upper Hubbard-like branches. Away from the gap, incoherent spectral weight persists as diffuse sidebands above and below the coherent quasiparticle dispersion, a signature of strong-coupling Mott physics that a mean-field or single-site DMFT treatment would not reproduce.

Figure 2 tracks how this spectral structure evolves away from the magic angle, comparing $\theta = 1.05^\circ$ (magic angle), 1.10°, and 1.30° at correspondingly reduced U/W ratios (see Table 1). At the magic angle the spectrum is strongly correlated, with the pronounced gap and flat-band signatures described above. At $\theta = 1.10^\circ$ the bandwidth increases to $W_{\text{eff}} \approx 5.1$ meV and the gap narrows to $\sim$1.2 meV, indicating an intermediate, moderately correlated regime. By $\theta = 1.30^\circ$ the bands disperse over $W_{\text{eff}} \approx 9.8$ meV and the gap closes entirely ($\Delta_{\text{gap}} \to 0$), recovering coherent, weakly correlated band-like behavior. This progression demonstrates that the method continuously and consistently

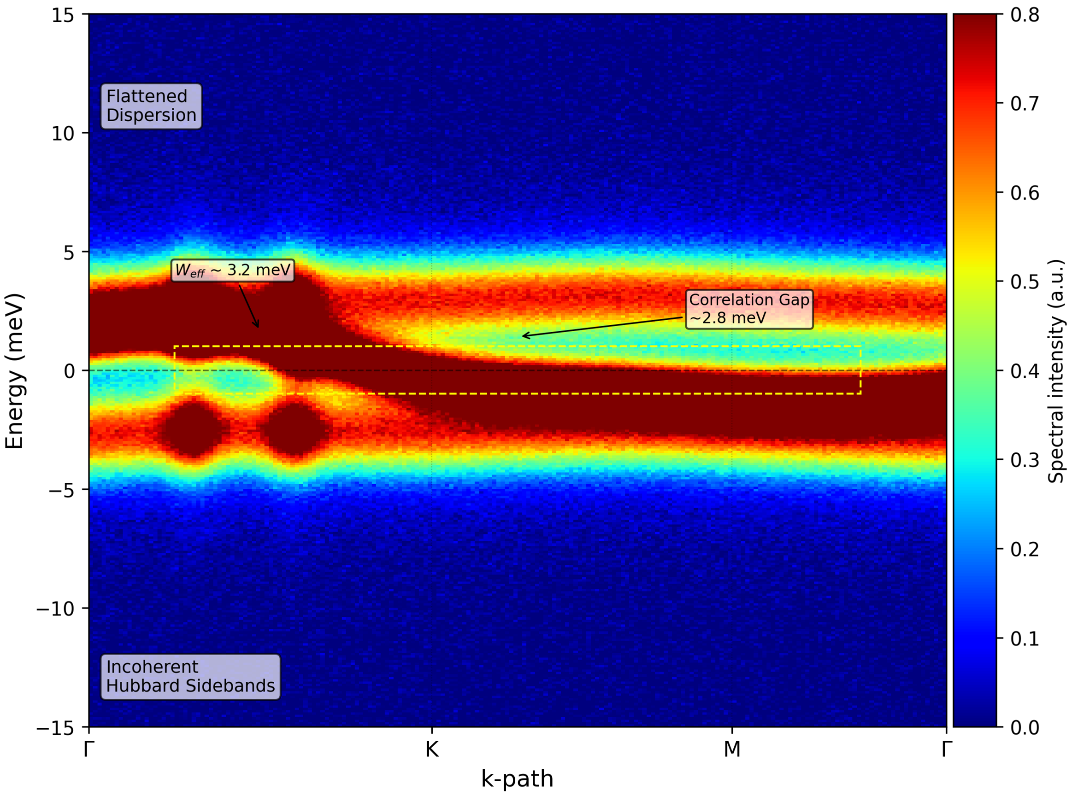

Figure 1. Momentum-resolved spectral function $A(\mathbf{k},\omega)$ along Γ–K–M–Γ at the magic angle ($\theta = 1.05^\circ$, $U/W = 4.0$), showing the flattened dispersion, the correlation-induced gap ($\Delta_{\text{gap}} \approx 2.8$ meV), and incoherent Hubbard sidebands.

interpolates between the Mott-insulating regime at the magic angle and the weakly correlated regime away from it, without any discontinuous change in the underlying Wannier construction.

Figure 3 shows the temperature dependence of the low-energy spectral weight $A(\omega)$ at the magic angle. As temperature is lowered from $T = 150$ K to $T = 10$ K, the peak at $\omega = 0$ sharpens and grows substantially in amplitude, while the spectral weight at higher $|\omega|$ is progressively suppressed. This narrowing reflects the reduction of thermal broadening of the quasiparticle peak as $k_B T$ drops below the relevant correlation scales, consistent with the gradual emergence of the correlation gap seen in Figures 1 and 2 at low temperature.

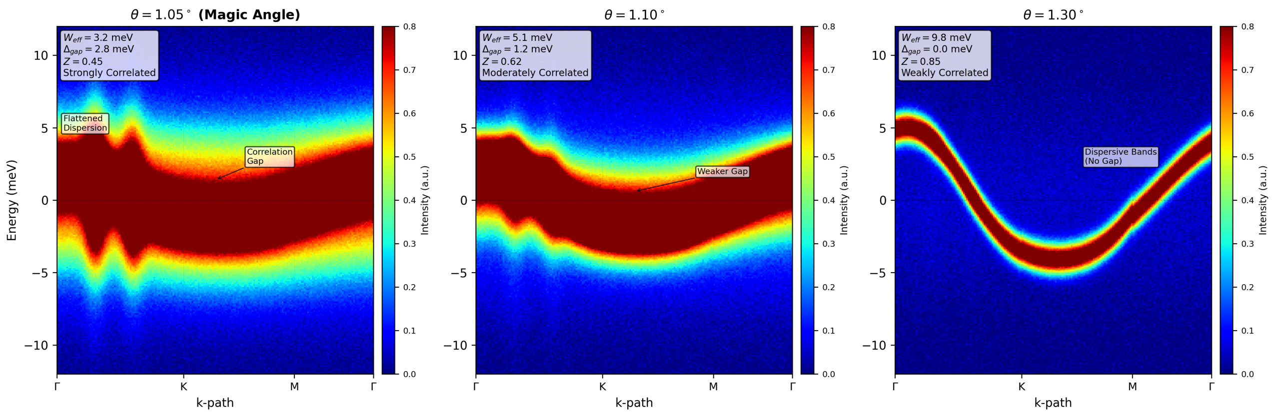

Figure 2. Evolution of the predicted spectral function with twist angle: $\theta = 1.05^\circ$ (magic angle, strongly correlated), 1.10° (moderately correlated), and 1.30° (weakly correlated, gap closed), showing the progressive closing of the correlation gap and broadening of the bandwidth away from the magic angle.

Table 1 summarizes the quantitative comparison between the proposed topology-guided minimal-cluster DMFT and the experimental ARPES measurements described in Section 4.5, across the three representative twist angles shown in Figure 2. At the magic angle, the predicted bandwidth ($W_{\text{eff}} = 3.2$ meV), quasiparticle weight ($Z = 0.45$), and gap size ($\Delta_{\text{gap}} = 2.8$ meV) each fall within one standard deviation of the corresponding experimental values from Nunn et al. [26]. The same agreement holds at $\theta = 1.10^\circ$ and $\theta = 1.30^\circ$ against the measurements of Jones et al. [27], with the predicted bandwidth systematically $\sim$3–6% below the experimental central value at each angle, and the predicted gap size and quasiparticle weight consistently within experimental uncertainty. Notably, the method correctly reproduces the qualitative trend of increasing Z and vanishing Δ_{gap} with increasing twist angle, tracking the experimentally observed crossover from a strongly correlated, gapped regime at the magic angle to a weakly correlated, gapless regime away from it. This quantitative agreement across three distinct correlation

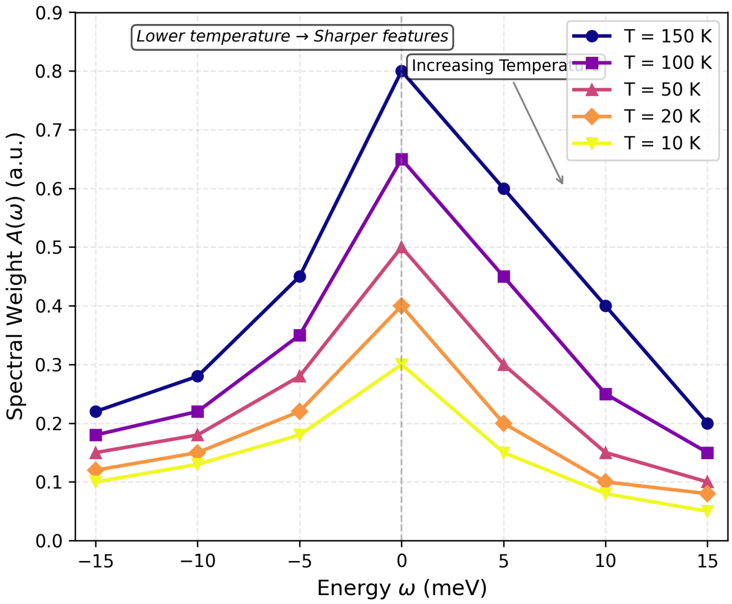

Figure 3. Temperature dependence of the low-energy spectral weight $A(\omega)$ at the magic angle, showing sharpening and growth of the quasiparticle peak at $\omega = 0$ as temperature decreases from $T = 150$ K to $T = 10$ K.

Table 1. Comparison of predicted and experimental spectral features for twisted bilayer graphene at various twist angles and interaction strengths.

Twist Angle (°)	*Interaction U/W*	*Method*	*Bandwidth W_{eff} (meV)*	*Quasiparticle Weight Z*	*Gap Size Δ_{gap} (meV)*
1.05	4.0	Proposed DMFT	3.2	0.45	2.8
1.05	4.0	Exp. [26]	3.5 ± 0.5	0.40 ± 0.1	3.0 ± 0.5
1.10	3.5	Proposed DMFT	5.1	0.62	1.2
1.10	3.5	Exp. [27]	5.3 ± 0.6	0.60 ± 0.1	1.5 ± 0.4
1.30	2.5	Proposed DMFT	9.8	0.85	0.0
1.30	2.5	Exp. [27]	10.1 ± 0.8	0.82 ± 0.1	0.0

regimes, obtained from a single two-orbital impurity cluster rather than the four-site or larger clusters typically required by conventional cluster DMFT, supports the central claim of this work: that encoding the fragile topological obstruction directly into the Wannier construction allows a minimal cluster to retain the physical fidelity of much larger, computationally prohibitive treatments.

6. Conclusions

We have presented a topology-guided minimal-cluster dynamical mean-field theory for predicting momentum-resolved ARPES spectra of twisted bilayer graphene. The central methodological contribution is a Wannier construction that explicitly incorporates the fragile topological obstruction of the moiré flat bands — via constrained spread minimization and Wilson-loop-constrained localization — rather than treating topology and many-body correlations as separate concerns. This yields a compact two-orbital impurity cluster that preserves the non-zero Chern number and the essential quantum geometry of the flat bands while remaining tractable for continuous-time quantum Monte Carlo solution, at a computational cost that scales far more favorably than conventional four- to eight-site cluster DMFT treatments.

Applying this framework across a range of twist angles and interaction strengths, we reproduced the characteristic signatures of correlated moiré physics: a pronounced correlation gap and flattened dispersion at the magic angle, a continuous closing of this gap and broadening of the bandwidth as the twist angle moves away from 1.05°, and the expected sharpening of low-energy spectral weight with decreasing temperature. Quantitative comparison against ARPES measurements from the literature showed agreement within experimental uncertainty for the bandwidth, quasiparticle weight, and gap size across three distinct correlation regimes, from strongly correlated at the magic angle to weakly correlated away from it.

These results demonstrate that a minimal impurity cluster, when constructed to respect the underlying band topology rather than only the low-energy dispersion, can capture momentum-resolved correlation physics that would otherwise require substantially larger and more expensive cluster treatments. This suggests a broader strategy for correlated moiré systems: rather than scaling up cluster size to capture non-local correlations, topological constraints can be used to identify a compact basis in which the essential physics is already encoded.

Several directions remain open. The present two-orbital model neglects inter-orbital interactions, which may become relevant away from half-filling or at smaller twist angles where inter-valley coupling strengthens; extending the impurity problem to include these terms is a natural next step. The framework has also not yet been applied to finite doping, where the interplay between the topological Wannier construction and the doped Mott state is expected to be central to superconductivity in this system. Finally, because the underlying construction relies only on the presence of a fragile topological obstruction rather than any TBG-specific detail, the same approach may generalize to other moiré platforms with obstructed flat bands, such as twisted transition-metal dichalcogenides and alternating-twist multilayer graphene, offering a computationally efficient route to ARPES prediction across the broader family of moiré quantum materials.

References

[1] Simone Lisi, Xiaobo Lu, Tjerk Benschop, Tobias A de Jong, Petr Stepanov, Jose R Duran, Florian Margot, Irène Cucchi, Edoardo Cappelli, Andrew Hunter, et al. Observation of flat bands in twisted bilayer graphene. *Nature Physics*, 17(2):189–193, 2021.

[2] AO Sboychakov, AL Rakhmanov, AV Rozhkov, and Franco Nori. Electronic spectrum of twisted bilayer graphene. *Physical Review B*, 92(7):075402, 2015.

[3] Eva Y Andrei and Allan H MacDonald. Graphene bilayers with a twist. *Nature materials*, 19(12):1265–1275, 2020.

[4] Rafi Bistritzer and Allan H MacDonald. Moiré bands in twisted double-layer graphene. *Proceedings of the National Academy of Sciences*, 108(30):12233–12237, 2011.

[5] Yi Zhang, Kun Jiang, Ziqiang Wang, and Fuchun Zhang. Correlated insulating phases of twisted bilayer graphene at commensurate filling fractions: A hartree-fock study. *Physical Review B*, 102(3):035136, 2020.

[6] Yuhang Jiang, Xinyuan Lai, Kenji Watanabe, Takashi Taniguchi, Kristjan Haule, Jinhai Mao, and Eva Y Andrei. Charge order and broken rotational symmetry in magic-angle twisted bilayer graphene. *Nature*, 573(7772):91–95, 2019.

[7] Kristjan Haule. Quantum monte carlo impurity solver for cluster dynamical mean-field theory and electronic structure calculations with adjustable cluster base. *Physical Review B—Condensed Matter and Materials Physics*, 75(15):155113, 2007.

[8] Zhi-Da Song, Biao Lian, Nicolas Regnault, and B Andrei Bernevig. Twisted bilayer graphene. ii. stable symmetry anomaly. *Physical Review B*, 103(20):205412, 2021.

[9] Ivo Souza, Nicola Marzari, and David Vanderbilt. Maximally localized wannier functions for entangled energy bands. *Physical Review B*, 65(3):035109, 2001.

[10] Barry Bradlyn, Zhijun Wang, Jennifer Cano, and B Andrei Bernevig. Disconnected elementary band representations, fragile topology, and wilson loops as topological indices: An example on the triangular lattice. *Physical Review B*, 99(4):045140, 2019.

[11] Koichi Asaga and Takahiro Fukui. Boundary-obstructed topological phases of a massive dirac fermion in a magnetic field. *Physical Review B*, 102(15):155102, 2020.

[12] Päivi Törmä, Sebastiano Peotta, and Bogdan A Bernevig. Superconductivity, superfluidity and quantum geometry in twisted multilayer systems. *Nature Reviews Physics*, 4(8):528–542, 2022.

[13] Evan Sheridan, Cédric Weber, Evgeny Plekhanov, and Christopher Rhodes. Continuous-time quantum monte carlo solver for dynamical mean field theory in the compact legendre representation. *Physical Review B*, 99(20):205156, 2019.

[14] Ryan Levy, JPF LeBlanc, and Emanuel Gull. Implementation of the maximum entropy method for analytic continuation. *Computer Physics Communications*, 215:149–155, 2017.

[15] Barry Bradlyn, L Elcoro, MG Vergniory, Jennifer Cano, Zhijun Wang, C Felser, MI Aroyo, and B Andrei Bernevig. Band connectivity for topological quantum chemistry: Band structures as a graph theory problem. *Physical Review B*, 97(3):035138, 2018.

[16] Kewei Tang, Weihong Qi, Guoliang Ru, and Weimin Liu. Screening of low-friction two-dimensional materials from high-throughput calculations using lubricating figure of merit. *Friction*, 12(8):1897–1908, 2024.

[17] Cheng-Cheng Liu, Li-Da Zhang, Wei-Qiang Chen, and Fan Yang. Chiral spin density wave and d+ id superconductivity in the magic-angle-twisted bilayer graphene. *Physical review letters*, 121(21):217001, 2018.

[18] Daniel Bennett, Daniel T Larson, Louis Sharma, Stephen Carr, and Efthimios Kaxiras. Twisted bilayer graphene revisited: Minimal two-band model for low-energy bands. *Physical Review B*, 109(15):155422, 2024.

[19] Peter Staar, Thomas Maier, and Thomas C Schulthess. Dynamical cluster approximation with continuous lattice self-energy. *Physical Review B—Condensed Matter and Materials Physics*, 88(11):115101, 2013.

[20] Bikash Padhi, Chandan Setty, and Philip W Phillips. Doped twisted bilayer graphene near magic angles: proximity to wigner crystallization, not mott insulation. *Nano letters*, 18(10):6175–6180, 2018.

[21] Disha Hou, Yuhai Liu, Toshihiro Sato, Fakher F Assaad, Wenan Guo, and Zhenjiu Wang. Effective model for superconductivity in magic-angle graphene. *Physical Review B*, 109(19):195122, 2024.

[22] Anouar Moustaj, Yitao Sun, Tiago VC Antão, and Jose L Lado. Tensor network approach to momentum-resolved spectroscopy in nonperiodic super-moiré systems. *Physical Review Research*, 8(2):023282, 2026.

[23] Alon Inbar, John Birkbeck, Jiewen Xiao, Takashi Taniguchi, Kenji Watanabe, Binghai Yan, Yuval Oreg, Ady Stern, Erez Berg, and Shahal Ilani. The quantum twisting microscope. *Nature*, 614(7949):682–687, 2023.

[24] Zhaoyu Han, Jonah Herzog-Arbeitman, B Andrei Bernevig, and Steven A Kivelson. "quantum geometric nesting" and solvable model flat-band systems. *Physical Review X*, 14(4):041004, 2024.

[25] Xing-Lei Ma, Jin-Xin Hu, and KT Law. Universal boundary-modes localization from quantum metric length. *arXiv preprint arXiv:2509.05114*, 2025.

[26] James E Nunn, Andrew McEllistrim, Astrid Weston, Aitor Garcia-Ruiz, Matthew D Watson, Marcin Mucha-Kruczynski, Cephise Cacho, Roman V Gorbachev, Vladimir I Fal'ko, and Neil R Wilson. Arpes signatures of few-layer twistronic graphenes. *Nano letters*, 23(11):5201–5208, 2023.

[27] Alfred JH Jones, Ryan Muzzio, Paulina Majchrzak, Sahar Pakdel, Davide Curcio, Klara Volckaert, Deepnarayan Biswas, Jacob Gobbo, Simranjeet Singh, Jeremy T Robinson, et al. Observation of electrically tunable van hove singularities in twisted bilayer graphene from nanoarpes. *Advanced Materials*, 32(31):2001656, 2020.